### Title

An improved analytical detector response function model for multilayer small-diameter PET scanners




### Journal

Physics in Medicine and Biology, 48(8)

### ISSN

0031-9155



### Authors

Strul, D
Slates, R B
Dahlbom, M
et al.



### Publication Date

2003-04-01

Peer reviewed

INSTITUTE OF PHYSICS PUBLISHING PHYSICS IN MEDICINE AND BIOLOGY

Phys. Med. Biol. **48** (2003) 979–994 PII: S0031-9155(03)57238-4

# An improved analytical detector response function model for multilayer small-diameter PET scanners

**D Strul[1,4], R B Slates[2], M Dahlbom[2], S R Cherry[3] and P K Marsden[1]**

[1] The Clinical PET Centre, Guy's, King's and St Thomas' School of Medicine, Lower Ground Floor, Lambeth Wing, St Thomas' Hospital, London SE1 7EH, UK
[2] Department of Molecular and Medical Pharmacology, Division of Nuclear Medicine, UCLA School of Medicine, 23-120 CHS, Box 951735, Los Angeles, CA 90095-1735, USA
[3] Department of Biomedical Engineering, University of California, Davis, 1026 Academic Surge, Davis, CA 95616-5294, USA

E-mail: paul.marsden@kcl.ac.uk

Received 6 December 2002
Published 1 April 2003
Online at stacks.iop.org/PMB/48/979

**Abstract**

The optimization of spatial resolution is a critical consideration in the design of small-diameter positron emission tomography (PET) scanners for animal imaging, and is often addressed with Monte Carlo simulations. As a faster and simpler solution, we have developed a new analytical model of the PET detector response function, and implemented the model for a small single-slice, multilayer PET scanner. The accuracy of the model has been assessed by comparison with both Monte Carlo simulations and experimental measurements published in the literature. Results from the analytical model agreed well with the Monte Carlo method, being noise free and two to three orders of magnitude faster. The only major discrepancy was a slight underestimation of the width of the point spread function by the analytical method as inter-crystal scatter is neglected. We observed good agreement between the predictions of the model and experimental measurements. For two large-diameter scanners additional discrepancies were seen due to photon acollinearity, which is not considered in the model. We have shown that the simple and fast analytical detector response function model can provide accurate estimates of spatial resolution for small-diameter PET scanners, and could be a useful tool for several applications, complementing or cross-validating other simulation methods.

[4] Present address: The PET Instrumentation Laboratory, Institute of High Energy Physics, University of Lausanne, 1015 Lausanne, Switzerland.

  

## 1. Introduction

Due to the small size of the structures to be studied, optimization of the tomographic spatial resolution is a critical issue for small-animal PET scanners. This is often addressed by using Monte Carlo methods to simulate the scanner point spread function (PSF), and thus assess the influence of various design parameters on the system resolution (Tsang *et al* 1995, Moses *et al* 1997, Pavlopoulos and Tzanakos 1997, Del Guerra *et al* 1998, Slates *et al* 1999). Monte Carlo simulations have numerous advantages, including their versatility and the possibility of modelling the physics of a PET scanner very precisely. However, they are also fairly slow, model dependent and very complex.

An alternative approach is to use an analytical detector response function (DRF) model (Keller and Lupton 1983, Lecomte *et al* 1984, Holmes and Ficke 1985, Schmitt *et al* 1986, 1988, Lecomte *et al* 1991, Karuta and Lecomte 1992). Such models, although less versatile than Monte Carlo simulations, have a number of advantages, as they are both noise free and very fast, allowing repeat simulations as often as required. Also, their relative simplicity allows a more direct appreciation of the influence of the parameters in the model.

In this paper, we present an analytical DRF model we have developed for the optimization of small-diameter PET scanners such as those used for small-animal imaging. A distinctive feature of this model is its ability to handle scanners with multiple crystal layers in the radial direction, a design often proposed for measuring the gamma ray depth-of-interaction (DOI) (e.g. Slates *et al* 1999, Inadama *et al* 2002, Saoudi *et al* 1999). Also, the transverse field-of-view (FOV) is allowed to represent a large fraction of the detector ring diameter, as may happen in many small-animal scanners (Garlick *et al* 1997, Shao *et al* 1997, Boning *et al* 2000). This is a major difference from models described previously in the literature (Holmes and Ficke 1985, Schmitt *et al* 1988) which are not valid for large FOV configurations.

In the first part of this paper, we summarize the theory of our analytical model, along with the most important features of its implementation. We then present the results of validation tests against a Monte Carlo simulation program and against data published in the literature for various scanners.

## 2. The analytical DRF model

### *2.1. Theory*

Our analytical DRF model is a development of those previously proposed in the literature (Lecomte *et al* 1984, Holmes and Ficke 1985, Schmitt *et al* 1988, Karuta and Lecomte 1992). It is based on a set of equations describing the efficiencies of the detection processes that take place during data acquisition. While these equations can generally not be solved analytically, they can be implemented into a multi-stage algorithm allowing the estimation of the detection efficiency for any crystal pair. The basic equations of this model are presented below, and some elements of their implementation are described in the next section.

Let us define a reference frame (O, $x$, $y$, $z$) attached to the scanner (figure 1), where O is the centre of the field-of-view, (O, $z$) is the scanner axis and (O, $x$, $y$) is the central plane of the scanner. In this reference frame, a given direction may be described either by a normalized vector $\mathbf{n}$ or by its spherical coordinates ($\theta$, $\varphi$), where $\theta \in [0, 2\pi]$ is the in-plane angle and $\varphi \in [0, \pi]$ is the out-of-plane angle made with the scanner axis.

Let us consider a flux of photons emitted by a source at a point $M$ along a direction $\mathbf{n}$ and reaching a crystal $c$ (figure 2). In the linear attenuation model, and in the absence

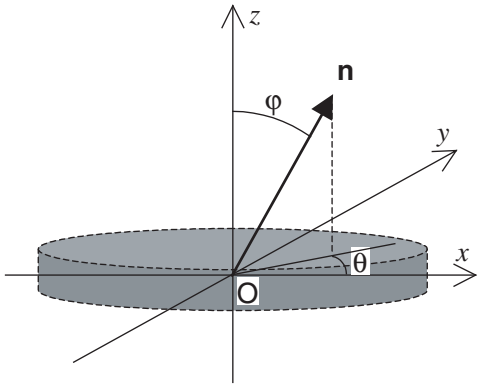


**Figure 1.** Reference frame used for the analytical model.

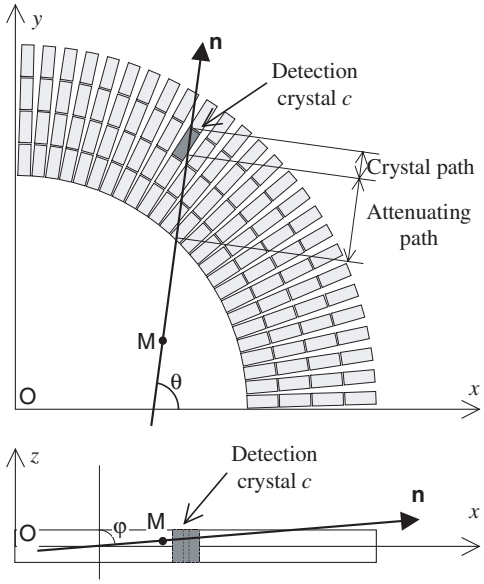


**Figure 2.** Simplified transverse (top) and lateral (bottom) views of the elements for the analytical model.

of a scattering medium within the field-of-view, the probability $p_c(M, \mathbf{n})$ of detecting these photons is assumed equal to the attenuation of the flux by the crystal:

$$p_c(M, \mathbf{n}) = \{1 - \exp[-\mu_c L_c(M, \mathbf{n})]\} A_c(M, \mathbf{n}). \tag{1}$$

In this expression, $\mu_c$ is the total (photoelectric + Compton) crystal attenuation coefficient, $L_c(M, \mathbf{n})$ is the path length of the photon flux across crystal $c$ and $A_c(M, \mathbf{n})$ represents the attenuation of the photon flux prior to entering $c$.

The latter term can be computed by taking into account the attenuating contribution of each component of the scanner (crystal, inter-crystal gap, septum, etc) traversed prior to entering $c$, and may be computed as

$$A_c(M, \mathbf{n}) = \exp\left[-\sum \mu_i L_i(M, \mathbf{n})\right] \tag{2}$$

where $\mu_i$ is the total attenuation coefficient and $L_i(M, \mathbf{n})$ is the path length of the photon flux in the $i$th component traversed by the photon flux before entering $c$.

Neglecting photon non-collinearity effects, each photon emitted along $\mathbf{n}$ is paired with an opposite photon emitted along $(-\mathbf{n})$. Consequently, the probability of coincident detection $p_{cd}(M, \mathbf{n})$, also denoted as $p_{cd}(M, \theta, \varphi)$, by a crystal pair $(c, d)$ of photon pairs emitted at $M$ along the direction $\mathbf{n}(\theta, \varphi)$, is simply the product of the crystal detection probabilities for the crystals $c$ and $d$:

$$p_{cd}(M, \mathbf{n}) = p_c(M, \mathbf{n})\, p_d(M, -\mathbf{n}). \tag{3}$$

From this expression, the total detection efficiency $\varepsilon_{cd}(M)$ for the crystal pair $(c, d)$, for emissions originating from the point $M$, is computed by integrating over all possible directions:

$$\varepsilon_{cd}(M) = \frac{1}{4\pi} \int_0^{2\pi} \int_0^{\pi} p_{cd}(M, \theta, \varphi) \sin\varphi \, \mathrm{d}\varphi \, \mathrm{d}\theta. \tag{4}$$

To separate in-plane effects from axial effects, the computation of this integral may be broken into two steps. Because the out-of-plane effects are often neglected, we will use the following decomposition:

$$\varepsilon_{cd}(M) = \frac{1}{2\pi} \int_0^{2\pi} p_{cd}(M, \theta, 0) \alpha_{cd}(M, \theta) \, \mathrm{d}\theta \tag{5}$$

with

$$\alpha_{cd}(M, \theta) = \frac{\frac{1}{2} \int_0^{\pi} p_{cd}(M, \theta, \varphi) \sin\varphi \, \mathrm{d}\varphi}{p_{cd}(M, \theta, 0)}. \tag{6}$$

In these expressions, $p_{cd}(M, \theta, 0)$ is the probability of detection of the photons emitted with an arbitrary in-plane angle $\theta$ and with a zero out-of-plane angle $\varphi$ (in-plane photons). Equation (5) gives the total detection efficiency for the crystal pair $(c, d)$ as a single integral of this probability $p_{cd}(M, \theta, 0)$, multiplied by an axial efficiency factor $\alpha_{cd}(M, \theta)$.

In a fully three-dimensional simulation, this factor would be computed using the integral equation (6). As this computation is cumbersome and time consuming, the problem is often restricted by considering a 2D model, where all out-of-plane effects are neglected. In this very simple situation, equation (6) must be rewritten in a slightly different way (taking into account the fact that all the photons are emitted in plane), and equation (5) reduces to

$$\varepsilon_{cd}(M) = \frac{1}{2\pi} \int_0^{2\pi} p_{cd}(M, \theta, 0) \, \mathrm{d}\theta. \tag{5'}$$

From this equation, detection efficiency for a given crystal pair and a given point source may be computed. By computing this efficiency for a continuum of source positions, it is possible to compute the detector response function of this detector pair, also called the coincident aperture function (Lecomte *et al* 1984, Holmes and Ficke 1985).

An alternative approach, which is used in our implementation of the model, is to consider a fixed source position $M$, compute $\varepsilon_{cd}(M)$ for all detector pairs, and store these detection efficiencies in the appropriate positions of a sinogram matrix. Used in this manner, the DRF model actually simulates a noise-free PET sinogram for the source at $M$. Such a sinogram may then be processed by a variety of algorithms (normalization, DOI correction, reconstruction) to simulate noise-free images.

Before discussing the implementation of the model, it is worth underlining the main properties. On the one hand, the DRF model described here does not make any assumption about the scanner geometry, and thus can be applied to very complex scanners. In particular, this model readily applies to multilayer scanners, provided that the attenuation $A_c(M, \mathbf{n})$

computed in equation (2) includes the contributions of the layers crossed by the photon flux before entering the crystal $c$. Also, it can handle geometries where the FOV is a large fraction of the scanner diameter, contrary to previous analytical models whose equations were further simplified based on the hypothesis that the field-of-view would only be a limited fraction of the scanner diameter.

On the other hand, along with earlier works, our DRF model does not take into account positron range, photon acollinearity or the influence of the crystal read-out. While it takes into account attenuation through Compton interactions, it does not consider the influence of secondary Compton-scattered photons. In its 2D form, because the axial aspects of the emission and detection process are not accounted for, it models a situation close, but not strictly identical, to that of a line source rather than that of a point source.

### *2.2. Computer implementation*

We have implemented the analytical DRF model in a C program that simulates a single-slice, multilayer PET scanner configuration. The crystals may be either rectangular or wedge shaped, and evenly spaced, so that the geometry of the scanner is invariant by a rotation of angle $\Delta\alpha = 2\pi/N$ (where $N$ is the number of crystals in one layer). For simplicity and computational efficiency, the analytical simulation programs currently implement the 2D form of the model. While the computations are directly based on the model equations presented above, several accelerating techniques have been used, which are briefly described below.

To compute a series of sinograms, it is necessary to loop over several variables, i.e. the source position $M$, the crystal pair $(c, d)$ and the emission angle $\theta$. In turn, each of these loops may comprise a large number of computational steps. For instance, the computation of a $128 \times 64$ sinogram, with equation (5′) being implemented as a sum over 180 angles, would require $p_{cd}(M, \theta, 0)$ to be computed 1.47 million times. The computation of this latter probability requires the computation of two single-crystal probabilities (one for each crystal of a pair), each of which requires the computation of several path lengths. Thus, the analytical computation of a full sinogram may involve a very large number of computational steps, especially for scanners with complex structures or with multiple crystal layers.

In our implementation, the computation is accelerated by using the properties of rotational invariance of the scanner geometry. Owing to this property, the only difference between one sinogram bin and the adjacent bin on the next sinogram line is that both detection crystals have been rotated by an angle $\Delta\alpha = 2\pi/N$ around the axis of the scanner. This is equivalent to maintaining the same crystal pair but rotating the source position $M$ by $(-\Delta\alpha)$ around the scanner axis. Using this property, it is only necessary to consider a limited subset of crystal pairs and emission angles. Also, the number of emission angles is minimized in the following manner. We initially select the crystal pair (of the first sinogram line) that has the smallest angular aperture (the span of angles under which a source could be seen by both detectors). An emission angle step $\Delta\theta$ is then computed as a fraction (typically one tenth) of this aperture. From then on, the detection efficiency for each crystal pair is computed as the sum of the detection probabilities $p_{cd}(M, i\Delta\theta, 0)$ for the emission angles $(i\Delta\theta)$ that are integer multiples of the angular step $\Delta\theta$ and are within the detector pair angular aperture, as shown in figure 3. Thus, typically only ten emission angles are needed for the lines-of-response near the centre of the FOV, and up to several hundreds of angles are used near the edge, where the crystal pair angular apertures are much larger.

For each emission angle $\theta$, the computation of the detection probabilities is accelerated by rotating the whole reference frame by $(-\theta)$, as shown in figure 4. In the rotated reference frame, the photon direction is horizontal, so that all the path lengths needed for equations (1)

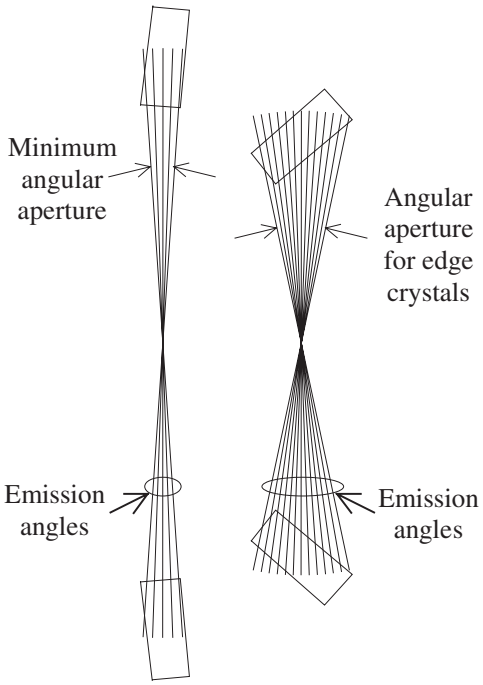


**Figure 3.** Angular apertures and sets of emission angles for a crystal pair near the centre (left) and edge (right) of the field-of-view.

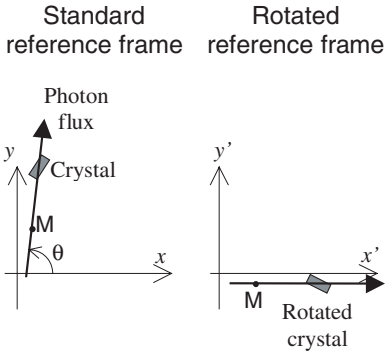


**Figure 4.** Principle used to accelerate the computation of the crystal detection probabilities. On the left is the standard reference frame, linked to the scanner axis. On the right is the rotated reference frame used for all path computations, where the photon direction is horizontal while the source and the crystal have been rotated by $(-\theta)$.

and (2) can be easily and quickly computed from the intersections of the photon trajectory with the crystal borders. The rotated geometry is used for all source positions and all crystal pairs of interest before proceeding to the next emission angle. (Note that the assumption of rotational invariance does of course limit the application of the model to scanners that have a ring geometry.)

Note that, for multilayer systems, the detection efficiencies must be computed not only for intra-layer but also for inter-layer lines-of-response. This is done using the approach of

MacDonald and Dahlbom (1998): for a PET scanner with $L$ layers, each simulation creates a multi-plane sinogram containing $L^2$ sinogram planes, each sinogram plane storing the detection efficiencies for a specific combination of layers. These planes are then merged into a composite monoplane sinogram using a parallax-correction algorithm, where all the sinogram planes are resampled and summed onto a common sampling grid.

In its standard mode, the analytical simulation program generates a full sinogram for one source at a given position. This sinogram may then be used to reconstruct a simulated image. To obtain profiles of the intrinsic radial and tangential PSFs at a given radius, simulations are repeated for a series of evenly spaced source locations, with only the first projection angle being computed for each source location. The results of these simulations are then stored in what will be denoted as an 'intrinsic sinogram', where each line corresponds to a different source location. Since each column of the intrinsic sinogram stores the detection efficiency for a given crystal pair and a series of source locations, it actually is a section of a PSF profile. Thus, the PSF profile for a given crystal pair is obtained by extracting the column of the intrinsic sinogram corresponding to this crystal pair.

## 3. Material and methods

We have compared the simulations generated by the analytical model with those obtained with a Monte Carlo simulation package. The latter program was developed at UCLA and has previously been applied to the design of small-animal scanners (Slates *et al* 1999). It accepts multi-layer scanner configurations, and takes into account the position and size of all crystals and inter-crystal gaps. It models photon acollinearity and Compton scattering, but not positron range. A model of a centroid crystal read-out is included, and it incorporates a global energy threshold (set to 350 keV) on the sum of all interaction energies. There is no electronic veto threshold (on the individual interaction energies) and no model of the crystal energy uncertainty (i.e. the detectors have perfect energy resolution).

The results from the analytical and the Monte Carlo methods were compared for several designs of single-slice, multi-layer, scanners employing lutetium oxyorthosilicate (LSO) scintillator, with internal ring radius 37 mm, external radius 57 mm and slice thickness 3 mm. These scanners consisted of one to four concentric crystal layers, each layer comprising 104, 2 mm wide, rectangular LSO crystals. The crystal length varied from one system to the other, being always set so that the total scintillating length would be 20 mm.

For each of these systems, both the Monte Carlo and analytical methods were used to compute the radial and tangential PSF at four measurement positions (0 mm, 10 mm, 20 mm and 30 mm) between the centre and the edge of the field-of-view. At each measurement position, two series of sources were used, one to simulate the tangential PSF and the other the radial PSF. For each Monte Carlo simulation (i.e. each source location), 10 million disintegrations were simulated. Intrinsic sinograms at these positions were then produced, either directly (by the analytical simulation program) or by extracting the first line of each full sinogram plane (for the Monte Carlo simulations). The intrinsic sinograms thus obtained comprised multiple planes, which were merged into composite monoplane sinograms using the parallax-correction algorithm of MacDonald and Dahlbom. The same correction algorithm was also used for the monolayer systems, since it is equivalent for such systems to a standard arc correction method. Beyond this parallax correction, the sinograms were not subject to any further processing (no normalization). The radial and tangential PSFs at each position were computed by extracting a single vertical profile from each intrinsic sinogram at the appropriate position. The radial and tangential full-width at half-maximum (FWHM) and full-width at tenth-maximum (FWTM) were then measured directly on these profiles.

For the Monte Carlo simulation, the tangential PSFs were generated using series of 31 source locations (0.1 mm apart) between −2 mm and +2 mm of each measurement position. Similarly, series of 23 source locations (0.5 mm apart) between −5 mm and +6 mm of each measurement position were used for the Monte Carlo radial PSFs. The analytical PSFs were computed using either the same series of sources or series with a step size ten times finer (301 and 221 source locations for the tangential and radial PSFs respectively).

To assess the physical accuracy of the analytical model, the Monte Carlo simulations for the four-layer design were repeated under different conditions: (1) standard Monte Carlo simulation, (2) Compton-scattered photons ignored, (3) 'first-hit' read-out with threshold at 510 keV, (4) photon acollinearity ignored. In the 'first-hit' condition, only the first crystals where the photons deposit energy are taken into account, all subsequent interactions being ignored. This condition is thus very similar to ignoring the Compton-scattered photons altogether (condition 2).

To assess the performance of our model in a wider range of designs, we have compared our results with those published in the literature for several scanners: the Donner 600 (Derenzo *et al* 1987), ECAT 713 (Cutler *et al* 1992), the Sherbrooke tomograph (Lecomte *et al* 1994) and MicroPET (Chatziioannou *et al* 1999). For each of these systems, we have run analytical simulations at the positions where intrinsic resolution data were available, and compared the simulated FWHMs with the published ones.

## 4. Results

### *4.1. Comparison with Monte Carlo simulations*

Figures 5 and 6 show some of the results obtained for the monolayer design. We observed a very good overall agreement between the two simulation methods. This agreement was especially good for the shape of the radial PSFs (figure 5). Some differences could be seen in the geometrical features of the tangential PSFs (figure 6), essentially regarding the shape of the central plateau and the presence or the absence of distribution tails. It is worth emphasizing that, contrary to the Monte Carlo approach, the analytical model provides simulations that are entirely noise free.

The good agreement between the two simulation methods was confirmed by the quantitative measures of resolution summarized in table 1. The tangential FWHM was nearly identical at all points for both methods, while the tangential FWTM was very slightly underestimated by the analytical algorithm (difference $<0.1$ mm). The difference was slightly higher for the radial resolution but remained fairly small, with the analytical algorithm underestimating the radial FWHM by less than 0.1 mm. The largest differences between the two simulations were found for the radial FWTMs, these differences reaching 0.3 mm at some points.

The results obtained for the designs with multiple crystal layers are fairly similar, as shown by figures 7 to 9. In particular, the tangential FWHMs and FWTMs were nearly identical for the two simulation methods with all the designs we tested (data not shown here). Similarly, the estimations of the radial FWHM were very close, the differences between the analytical and Monte Carlo methods remaining below 0.2 mm (figure 8). As previously, larger discrepancies were found for the radial FWTM, which was systematically underestimated by the analytical simulation by up to 0.6 mm (figure 9).

The reasons for these differences are made clearer if one examines the results obtained when the parameters of the Monte Carlo simulation are changed, as shown in figure 10 and table 2. It can be seen that the main cause of discrepancy between the methods is the

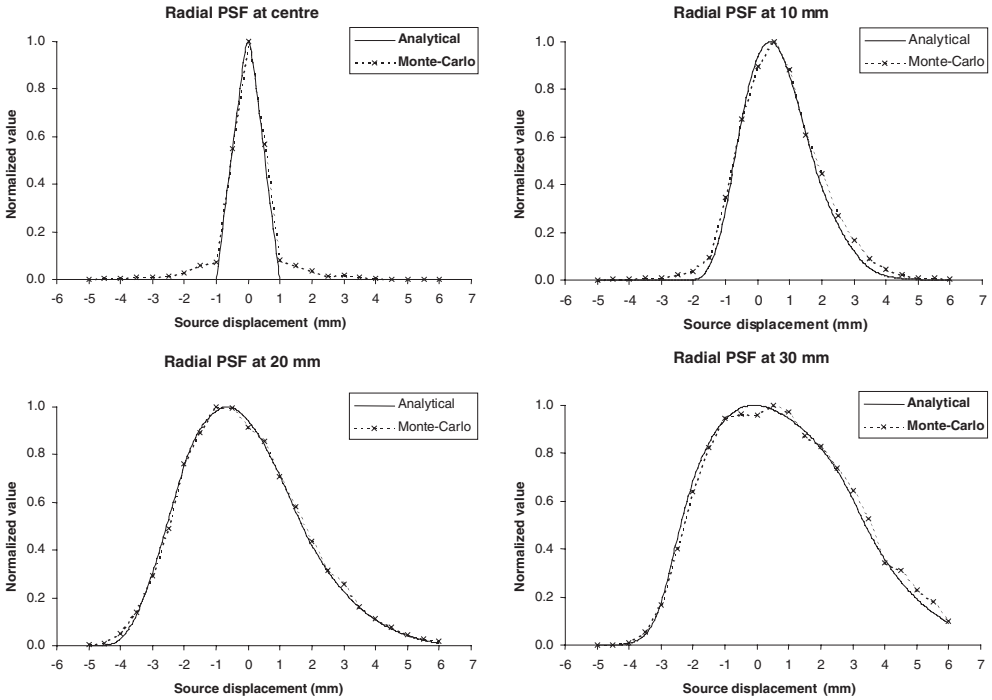


**Figure 5.** Comparison of the radial PSFs obtained by analytical and Monte Carlo simulation for a monolayer system at four positions between 0 and 30 mm off-centre.

**Table 1.** Comparison of the FWHMs and FWTMs measured for a monolayer system.

| | FWHM (FWTM) in mm | | | |
|---|---|---|---|---|
| | Tangential | | Radial | |
| Position | Monte Carlo | Analytical | Monte Carlo | Analytical |
| Centre | 1.1 (1.9) | 1.1 (1.8) | 1.1 (1.9) | 1.0 (1.8) |
| 10 mm off-centre | 1.2 (1.9) | 1.2 (1.8) | 2.6 (4.9) | 2.5 (4.6) |
| 20 mm off-centre | 1.4 (2.0) | 1.5 (1.9) | 4.2 (7.9) | 4.3 (7.8) |
| 30 mm off-centre | 1.7 (2.0) | 1.7 (1.9) | 5.8 (9.3) | 5.7 (9.1) |

inter-crystal scatter. This effect, caused by the detection of the Compton-scattered photons, is responsible for the presence of the tails on the Monte Carlo PSF profiles, and for the enlargement of the FWTMs and the radial FWHMs. When this effect is removed by neglecting the Compton-scattered photons or by using a first-hit read-out scheme, the agreement between the two simulation methods becomes nearly perfect. Due to the small diameter of the systems considered here, the effects of photon acollinearity are almost negligible.

Some more subtle differences between the two simulation methods may be seen by computing the pixel-by-pixel ratio of sinograms obtained from Monte Carlo and analytical simulations for an offset source, as shown in figure 11. This ratio varies slowly across the sinogram, being greatest towards the top and the bottom and minimal towards the middle. This occurs because of the two-dimensional approximation employed in the analytical model. The detection efficiency for a given source and a given crystal pair is determined by equation (5′) only, and is independent of the axial angular aperture subtended at the source by the crystal

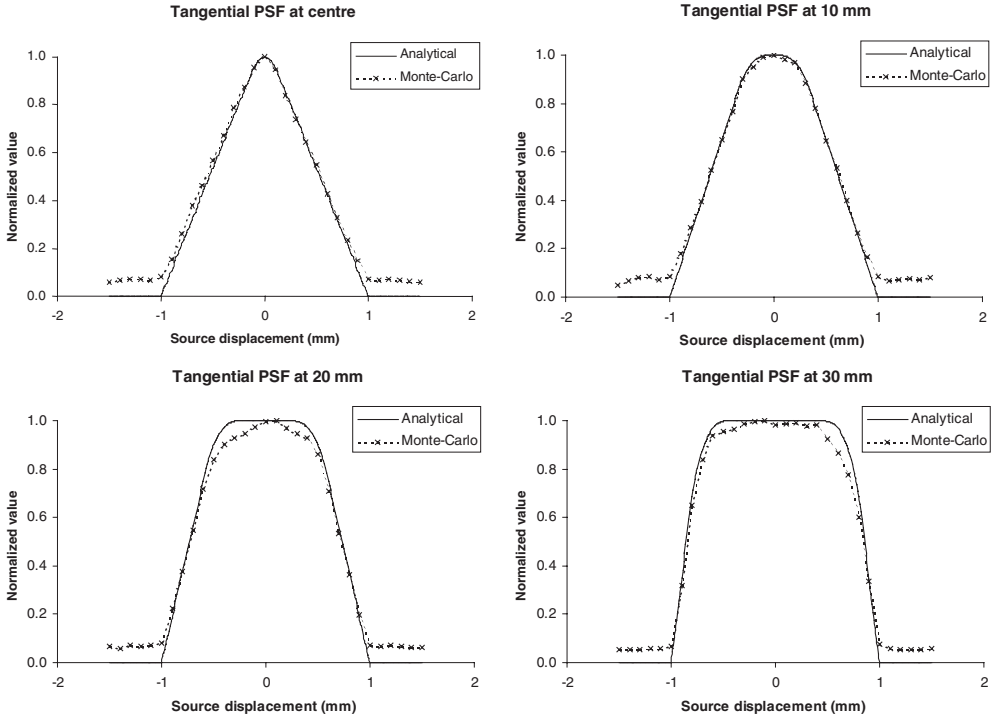


**Figure 6.** Comparison of the tangential PSFs obtained by analytical and Monte Carlo simulation for a monolayer system at four positions between 0 and 30 mm off-centre.

**Table 2.** Comparison of the FWHMs and FWTMs measured for a 4-layer system with different Monte-Carlo conditions.

| | FWHM (FWTM) in mm | | |
|---|---|---|---|
| Simulation condition | Centre | Tangential at 30 mm | Radial at 30 mm |
| Analytical | 1.1 (1.8) | 1.7 (1.9) | 2.2 (3.9) |
| Standard Monte Carlo | 1.1 (2.0) | 1.7 (2.0) | 2.4 (4.4) |
| No Compton scattered photons | 1.1 (1.8) | 1.7 (1.9) | 2.2 (3.9) |
| First-hit read-out | 1.0 (1.8) | 1.7 (1.9) | 2.2 (3.9) |
| No photon non-collinearity | 1.1 (1.9) | 1.7 (2.0) | 2.3 (4.4) |

pair. In the three-dimensional Monte Carlo model, the axial detection efficiency increases with the axial detection aperture. Consequently the ratio between the Monte Carlo and the analytical sinogram increases with the axial detection aperture being maximal when the source lies halfway between the two crystals of each pair (top and bottom of sinogram). Note that this variation of the detection efficiency is very slow, and so is not likely to influence much the shape of the intrinsic PSFs, the width of which are typically much smaller than the diameter of the FOV.

The computation time for the Monte Carlo simulation was independent of the number of layers, taking about 1 day in total on a Sun Ultra 10 workstation. The analytical simulation time increased with the number of layers, but always remained between 100 and 1000 times lower.

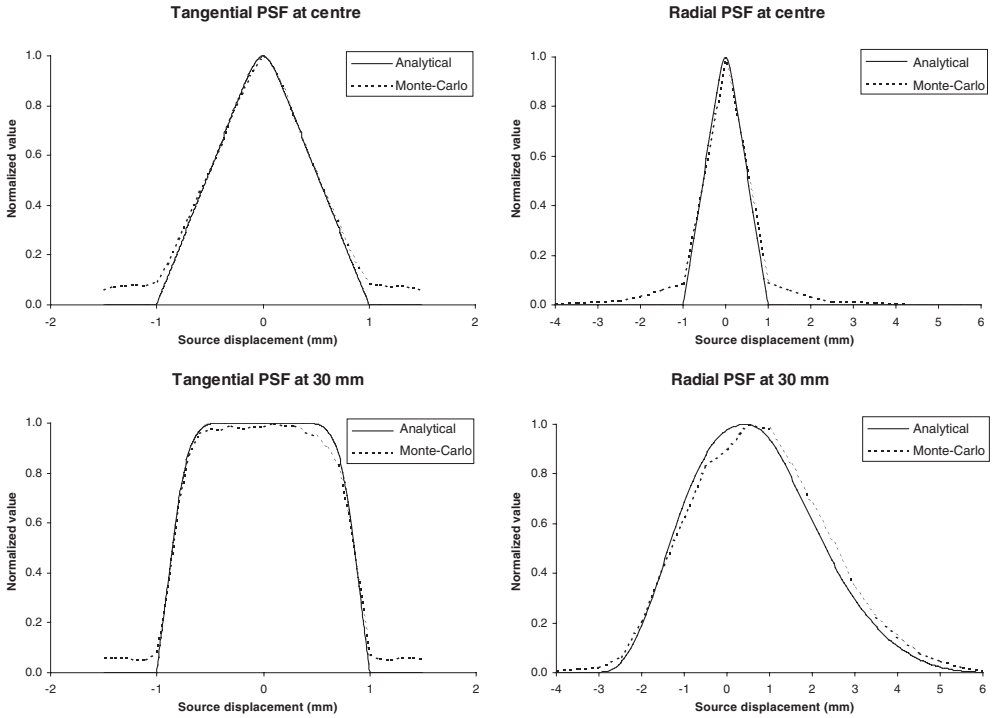


**Figure 7.** Tangential (left) and radial (right) PSFs simulated at the centre and at 30 mm for a dual-layer system.

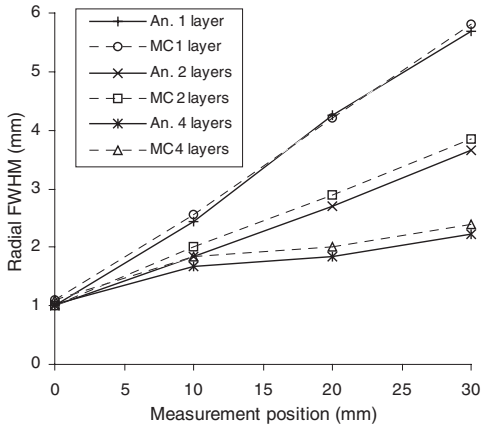


**Figure 8.** Radial FWHM throughout the field-of-view for systems with one, two or four layers of crystals, as estimated by the analytical (An) and Monte Carlo (MC) methods.

It is worth noting that we had initially performed a series of tests to determine the optimal number of disintegrations for the Monte Carlo simulation (data not shown here). We found out that the value of 10 million disintegrations used here was an absolute minimum for our systems, as lower values lead to unacceptable levels of noise in the final PSF. More robust estimates of the FWHM and the FWTM by the Monte Carlo method would actually need even higher statistics, requiring computation times of several days.

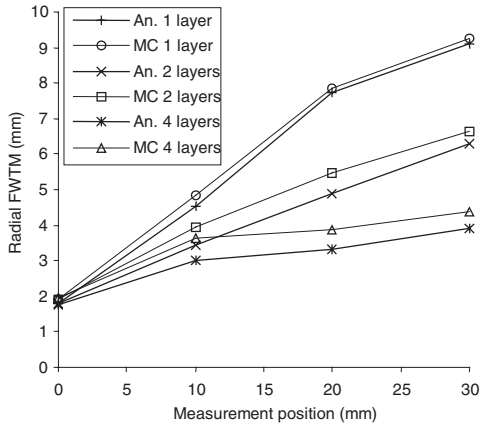


**Figure 9.** Radial FWTM throughout the field-of-view for systems with one, two or four layers of crystals, as estimated by the analytical (An) and Monte Carlo (MC) methods.

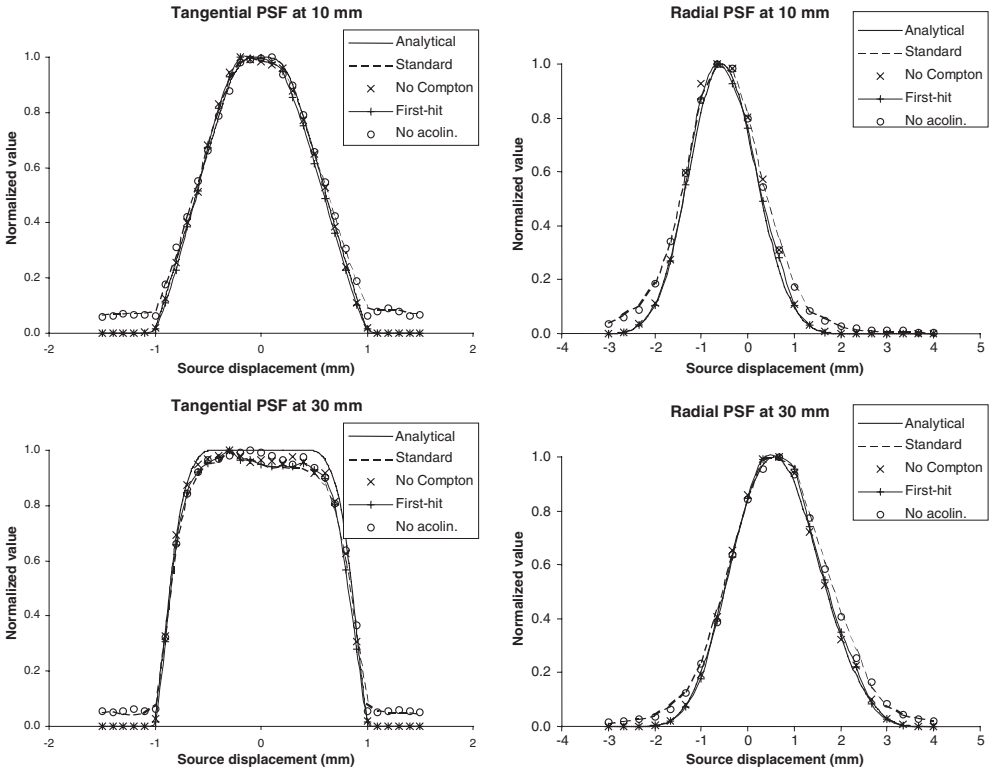


**Figure 10.** Comparison of the analytical and Monte Carlo simulations for a four-layer system with different Monte Carlo conditions.

The results of the comparison between the analytical simulations and the published data are summarized in figure 12. As may be seen, the analytical simulation very slightly underestimates the radial resolution at the centre for the MicroPET and Sherbrooke systems. For the Donner 600, there is good agreement between the simulations and the values found

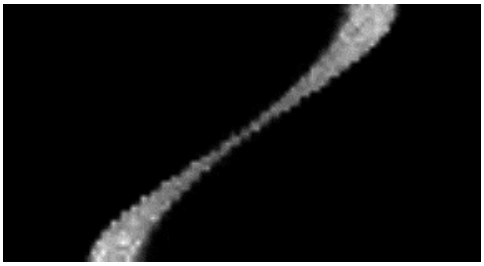

**Figure 11.** Pixel-by-pixel ratio of a Monte Carlo sinogram to an analytical one.

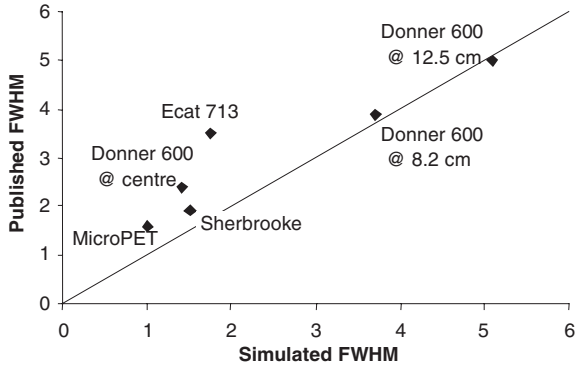


**Figure 12.** Comparison of the simulated spatial resolutions with resolution data published in the literature. For the MicroPET, ECAT 713 and Sherbrooke tomograph, the resolutions were computed at the centre.

in the literature at 8.2 and 12.5 cm off-centre. In contrast, significant discrepancies are observed for the Donner 600 at the centre (simulated FWHM = 1.4 mm versus experimental FWHM = 2.4 mm) and even more for the ECAT 713 (simulated = 1.76 mm versus experimental = 3.5 mm).

The Donner 600 and the ECAT 713 both have significantly larger ring diameters (60 cm and 64 cm respectively) than the MicroPET and the Sherbrooke systems (17.2 cm and 31 cm respectively). Their FWHM at the centre is thus enlarged by the effects of photon acollinearity (Gaussian distribution, width = 1.3 mm for a diameter of 60 cm), which may account for the observed discrepancy. The use of light-sharing block detectors in the ECAT 713 also probably plays a role in the large discrepancy observed for this scanner, as these blocks are known to further degrade the resolution (contribution of 1 to 2 mm). This cannot account for the discrepancy for the Donner 600, however, as this uses individual crystal read-out.

## 5. Discussion

Although analytical DRF models were proposed in the early eighties (Lecomte *et al* 1984, Holmes and Ficke 1985), Monte Carlo methods are generally preferred, as they are expected to be significantly more accurate. However, analytical models have interesting properties, mainly their ability to provide noise-free simulations and their very high computation speed. They also make it easier to obtain an intuitive understanding of the phenomena taking place.

In the work presented here, we have developed and implemented an extension of earlier analytical models to multilayer small-diameter PET scanners. We have assessed this model by comparison with both Monte Carlo simulations and experimental measurements published in the literature. We found that the point spread functions and the FWHMs obtained with the analytical model were satisfactory in most cases. For the small-diameter systems, limited discrepancies were found for the radial FWHM, primarily because inter-crystal scatter is ignored in the analytic model. Significant discrepancies were observed in only two cases, due to the enlarging of the PSF by various physical effects not taken into account by the model (positron range, photon non-collinearity, block read-out). We also observed in most cases significant discrepancies concerning the PSF distribution tails and the estimation of the FWTM. However, this result was indeed expected, since the analytical model is intrinsically unable to model inter-crystal scatter.

On the whole, analytical models seem extremely well suited to the optimization of small-animal PET scanners in terms of intrinsic resolution (FWHM), both with single and with multiple crystal layers. The high accuracy obtained is in part related to the small diameter of these systems, which limits the resolution loss due to photon acollinearity to a very small contribution ($\sim$0.2 mm at centre for a 10 cm diameter tomograph (Moses and Derenzo 1993, Derenzo *et al* 1993)). Also, small-animal scanners typically have rather short crystals ($<$20 mm), which limits the resolution loss by inter-crystal scatter to a fairly small level (Shao *et al* 1996, Levin *et al* 1997).

Some of the limitations encountered here could be overcome by further refinements, and the model could be adapted to larger ring diameters by modelling the photon acollinearity by rewriting equation (3) as an integral sum taking into account the distribution of angles between one photon and the opposite one. This was indeed implemented in an earlier version of our program and does not pose any major difficulty, but typically increases the computation time by a factor of 10 or more. Similarly, the model we have implemented is only two dimensional, and could easily be extended to fully three dimensional by implementing (6) with a significant increase in computation time. A more efficient approach may be to use a simplified model of the axial efficiency factor $\alpha_{cd}(M, \theta)$, allowing the computation of this factor from the axial angular aperture and avoiding the need to calculate the integral sum of equation (6).

Other refinements that can be readily incorporated into Monte Carlo models (i.e. inter-crystal scatter, crystal read-out and the effects of positron range) cannot be included in analytical DRF models in a straightforward way. Based on the findings of our work and that in the literature, however, we believe that analytical DRF models could prove extremely useful for a variety of applications. As demonstrated here, they could complement or cross-validate Monte Carlo methods for the design of PET scanners, especially during the first stage, where a large number of simulations are often needed to select basic design features.

Also, because they could allow resolution plots to be computed at a high number of closely located positions, analytical methods are probably better suited than Monte Carlo methods for the optimization of reconstruction algorithms, as they allow the detection and study of sampling effects and reconstruction-related artefacts.

Another potential application is the computation of the projection matrices needed by restorative iterative algorithms such as OS-EM. For these applications, the projection matrix is theoretically required for every pixel of the FOV. The computation of these projectors, generally done by Monte Carlo methods or from line-source measurements, is thus a very time consuming task (Boning *et al* 2000, Brix *et al* 1997). Analytical models can provide a much more efficient solution, as was demonstrated by Selivanov *et al* (2000).

Similarly, anatomically-guided partial volume effect (PVE) corrections, such as the GM-PET or ROI-PET methods, are dependent on noise-free simulation methods to simulate the

tomographic image blurring (Müller-Gärtner *et al* 1992, Rousset *et al* 1998). Most often, this processing is achieved by Gaussian smoothing, but the low accuracy of this method is a major problem for PVE correction, especially for pixel-by-pixel methods (Strul and Bendriem 1999, Meltzer *et al* 1999). Analytical DRF simulations, which are both quick, noise-free and realistically model the scanner physics, could provide an efficient solution to this problem.

## 6. Conclusion

We have assessed our analytical DRF by comparison with both Monte Carlo simulations and experimental measurements published in the literature. We found that the analytical simulation agreed well with the Monte Carlo method, while being both noise free and 100 to 1000 times faster. The only major discrepancy between the two methods was that the analytical model slightly underestimates the FWHM, as it neglects inter-crystal scatter. We also observed good agreement between the analytical simulations and experimental measurements in most cases, yet with significant discrepancies appearing in two cases of large-ring scanners, due to the enlarging of the PSF by various physical effects not taken into account by the model. Our results show that analytical DRF models can provide resolution estimates with a satisfactory accuracy for small animal PET scanners, and thus could be a very useful tool for a variety of applications, where they could complement or cross-validate other simulation methods.

## Acknowledgments

We thank William Hallett for his help in the validation of this algorithm. This work was supported by a grant from the Engineering and Physical Sciences Research Council.

## References

Boning G, Pichler B J, Rafecas M, Lorenz E, Schwaiger M and Ziegler S I 2000 Implementation of Monte Carlo coincident aperture functions in image generation of a high resolution animal positron tomograph *2000 IEEE Nuclear Science Symposium and Medical Imaging Conference (Lyon, France, 15–20 October 2000)*

Brix G, Doll J, Bellemann M E, Trojan H, Haberkorn U, Schmidlin P and Ostertag H 1997 Use of scanner characteristics in iterative image reconstruction for high-resolution positron emission tomography studies of small animals *Eur. J. Nucl. Med.* **24** 779–86

Chatziioannou A F, Cherry S R, Shao Y P, Silverman R W, Meadors K, Farquhar T H, Pedarsani M and Phelps M E 1999 Performance evaluation of microPET: a high-resolution lutetium oxyorthosilicate PET scanner for animal imaging *J. Nucl. Med.* **40** 1164–75

Cutler P D, Cherry S R, Hoffman E J, Digby W M and Phelps M E 1992 Design features and performance of a PET system for animal research *J. Nucl. Med.* **33** 595–604

Del Guerra A, DiDomenico G, Scandola M and Zavattini G 1998 High spatial resolution small animal YAP-PET *Nucl. Instrum. Methods* A **409** 537–41

Derenzo S E, Huesman R H, Cahoon J L, Geyer A, Uber D, Vuletich T and Budinger T F 1987 Initial results from the Donner-600 crystal positron tomograph *IEEE Trans. Nucl. Sci.* **34** 321–5

Derenzo S E, Moses W W, Huesman R H and Budinger T F 1993 Critical instrumentation issues for resolution smaller than 2 mm, high sensitivity brain PET *Quantification of Brain Function. Tracer Kinetics and Image Analysis in Brain PET* ed K Uemura, N A Lassen, T Jones and I Kanno (Amsterdam: Elsevier) pp 25–37

Garlick P B, Marsden P K, Cave A C, Parkes H G, Slates R, Shao Y, Silverman R W and Cherry S R 1997 PET and NMR dual acquisition (PANDA): applications to isolated, perfused rat hearts *NMR Biomed.* **10** 138–42

Holmes T J and Ficke D C 1985 Analysis of positron-emission tomography scintillation-detectors with wedge faces and inter-crystal septa *IEEE Trans. Nucl. Sci.* **32** 826–30

Inadama N, Murayama H, Omura T, Yamashita T, Yamamoto S, Ishibashi H, Kawai H, Omi K, Umehara T and Kasahara T 2002 A depth of interaction detector for PET with GSO crystals doped with different amounts of Ce *IEEE Trans. Nucl. Sci.* **49** 629–33

Karuta B and Lecomte R 1992 Effect of detector weighting functions on the point spread function of high-resolution PET tomographs—a simulation study *IEEE Trans. Med. Imaging* **11** 379–85

Keller N A and Lupton L R 1983 PET detector ring aperture function calculations using Monte-Carlo techniques *IEEE Trans. Nucl. Sci.* **30** 676–80

Lecomte R, Cadorette J, Richard P, Rodrigue S and Rouleau D 1994 Design and engineering aspects of a high resolution positron tomograph for small animal imaging *IEEE Trans. Nucl. Sci.* **41** 1446–52

Lecomte R, Martel C and Cadorette J 1991 Study of the resolution performance of an array of discrete detectors with independent readouts for positron emission tomography *IEEE Trans. Med. Imaging* **10** 347–57

Lecomte R, Schmitt D and Lamoureux G 1984 Geometry study of a high-resolution PET detection system using small detectors *IEEE Trans. Nucl. Sci.* **31** 556–61

Levin C S, Tornai M P, Cherry S R, MacDonald L R and Hoffman E J 1997 Compton scatter and X-ray crosstalk and the use of very thin intercrystal septa in high-resolution PET detectors *IEEE Trans. Nucl. Sci.* **44** 218–24

MacDonald L R and Dahlbom M 1998 Parallax correction in PET using depth of interaction information *IEEE Trans. Nucl. Sci.* **45** 2232–7

Meltzer C C, Kinahan P E, Greer P J, Nichols T E, Comtat C, Cantwell M N, Lin M P and Price J C 1999 Comparative evaluation of MR-based partial-volume correction schemes for PET *J. Nucl. Med.* **40** 2053–65

Moses W W and Derenzo S E 1993 Empirical observation of resolution degradation in positron emission tomographs utilizing block detectors *J. Nucl. Med.* **34** 101P

Moses W W, Virador P R G, Derenzo S E, Huesman R H and Budinger T F 1997 Design of a high-resolution, high-sensitivity PET camera for human brains and small animals *IEEE Trans. Nucl. Sci.* **44** 1487–91

Müller-Gärtner H W, Links J M, Prince J L, Bryan R N, McVeigh E, Leal J P and Frost J J 1992 Measurement of radiotracer concentration in brain grey matter using positron emission tomography: MRI-based correction for partial volume effects *J. Cereb. Blood Flow Metab.* **12** 571–83

Pavlopoulos S and Tzanakos G 1997 Design and performance evaluation of a high-resolution small animal positron tomograph *IEEE Trans. Nucl. Sci.* **43** 3249–55

Rousset O G, Ma Y and Evans A C 1998 Correction for partial volume effects in PET: principle and validation *J. Nucl. Med.* **39** 904–11

Saoudi A, Pepin CM, Dion F, Bentourkia M, Lecomte R, Andreaco M, Casey M, Nutt R and Dautet H 1999 Investigation of depth-of-interaction by pulse shape discrimination in multicrystal detectors read out by avalanche photodiodes *IEEE Trans. Nucl. Sci.* **46** 462–7

Schmitt D, Karuta B, Carrier C and Lecomte R 1988 Fast point spread function computation from aperture functions in high-resolution positron emission tomography *IEEE Trans. Med. Imaging* **7** 2–12

Schmitt D, Lecomte R and Lebel E 1986 Wedge-shaped scintillation crystals for positron emission tomography *J. Nucl. Med.* **27** 99–104

Selivanov V V, Picard Y, Cadorette J, Rodrigue S and Lecomte R 2000 Detector response models for statistical iterative image reconstruction in high resolution PET *IEEE Trans. Nucl. Sci.* **47** 1168–75

Shao Y, Cherry S R, Farahani K, Slates R, Silverman R W, Meadors K, Bowery A, Siegel S, Marsden P K and Garlick P B 1997 Development of a PET detector system compatible with MRI/NMR systems *IEEE Trans. Nucl. Sci.* **44** 1167–71

Shao Y, Cherry S R, Siegel S and Silverman R W 1996 A study of inter-crystal scatter in small scintillator arrays designed for high resolution PET imaging *IEEE Trans. Nucl. Sci.* **43** 1938–44

Slates R, Cherry S, Boutefnouchet A, Shao Y P, Dahlbom M and Farahani K 1999 Design of a small animal MR compatible PET scanner *IEEE Trans. Nucl. Sci.* **46** 565–70

Strul D and Bendriem B 1999 Robustness of anatomically guided pixel-by-pixel algorithms for partial volume effect correction in positron emission tomography *J. Cereb. Blood Flow Metab.* **19** 547–59

Tsang G, Moisan C and Rogers J G 1995 A simulation to model position encoding multicrystal PET detectors *IEEE Trans. Nucl. Sci.* **42** 2236–43